Vol. 27 • No. 1 • January 7 • 2015

www.advmat.de

ADVANCED MATERIALS

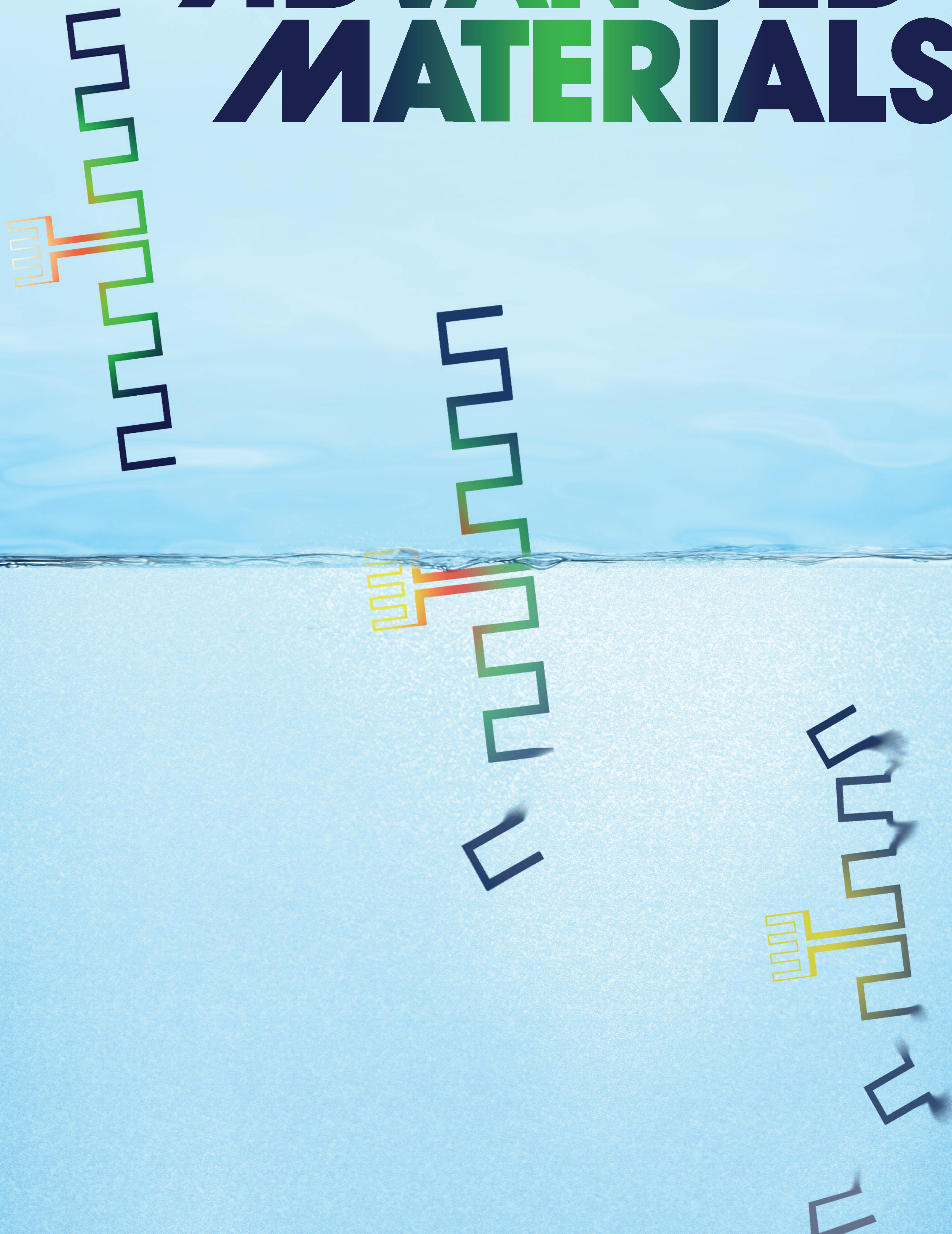

WILEY-VCH

Materials for Programmed, Functional Transformation in Transient Electronic Systems

*Suk-Won Hwang, Seung-Kyun Kang, Xian Huang, Mark A. Brenckle, Fiorenzo G. Omenetto, and John. A. Rogers**

Electronic systems that offer reliable, high-performance operation but are built using water-soluble, harmless materials have important potential applications in temporary biomedical implants, degradable environmental monitors/sensors, disposable "green" electronics, and hardware-secure systems.[1–12] Such technology can be viewed as a sub-set of a broader class of physically 'transient' electronics, in which some part or all of the systems are designed to disappear in a controlled manner through a physical and/or chemical process. The most advanced biodegradable, biocompatible systems exploit nanomembranes (NMs) of single-crystalline silicon (Si NMs)[6,11,13–16] or thin films of zinc oxide (ZnO)[17] as semiconductors, with metals such as Mg, Fe, Zn, W, or Mo for electrodes/interconnects,[12,18] MgO and SiO_2 or SiN_x for gate/interlayer dielectrics and encapsulation layers,[19] and silk fibroin, poly lactic-*co*-glycolic acid (PLGA), polycaprolactone (PCL) or poly(lactic acid) (PLA) for substrates/packaging materials.[11] Examples of reported devices built with these materials range from simple active components and logic gates (e.g., Si diodes,[6,13] n- and p-channel transistors,[6,11,13] and complementary metal-oxide-semiconductor (CMOS) inverters,[11,13] to integrated systems (e.g., strain/temperature/hydration sensors,[6,11] solar cells,[6] arrays of photodetectors,[6] mechanical energy harvesters (MEH)[17] and wireless RF power scavengers.[13] In all cases, dissolution of the substrate and encapsulating layers defines the operational lifetime. In the present work, we introduce a strategy in which spatial variations in the thicknesses and types of these and other constituent materials determine a time sequence for the dissolution of different components and sub-systems across the area of an integrated device. This process enables multi-staged transformation of functional behavior, with well-defined engineering control. Such capabilities qualitatively extend the design options and potential applications of transient electronics.

Dr. S.-W. Hwang, Dr. S.-K. Kang, Dr. X. Huang
Department of Materials Science and Engineering
Frederick Seitz Materials Research Laboratory
University of Illinois at Urbana-Champaign
Urbana, IL 61801, USA
Dr. S.-W. Hwang, KU-KIST Graduate School of
Converging Science and Technology,
Korea University
Seoul 136-701, Korea
Dr. X. Huang
Department of Mechanical and Aerospace Engineering.
Missouri University of Science and Technology, Rolla, MO, 65409, USA
M. A. Brenckle, Prof. F. G. Omenetto, Department of Biomedical
Engineering, Tufts University, Medford, MA, 02155, USA
Prof. J. A. Rogers, Department of Materials Science and
Engineering, Chemistry, Mechanical Science and Engineering
Electrical and Computer Engineering, Beckman Institute for
Advanced Science and Technology, and Frederick Seitz Materials
Research Laboratory
University of Illinois at Urbana-Champaign,
Urbana, IL, 61801, USA
E-mail: jrogers@illinois.edu

DOI: 10.1002/adma.201403051

Figure 1a presents schematic illustrations and circuit diagrams of an array of transient complementary metal-oxide-semiconductor (CMOS) NOR and NAND gates. The n- and p-channel metal-oxide-semiconductor field-effect transistors (MOSFETs) use Si NMs (ca. 260 nm) with Fe (ca. 300 nm) for source, drain, gate electrodes and interconnects, and MgO (ca. 80 nm) for the gate dielectrics. Certain regions of the interconnects incorporate Mg alloy (AZ31B) (ca. 100 nm) as the conductor. Beta-sheet crystallized films of regenerated silk fibroin serve as the substrate.[20] All of these materials are biodegradable and nontoxic.[6,15] Circuit fabrication involves forming lightly doped p-wells (p^-), and heavily doped n^+ and p^+ regions for contacts in the Si NMs for each type of MOSFET (n- and p-type), as described in detail elsewhere.[11,13] Transfer printing these doped Si NMs onto a thin layer of crystallized silk coated on a glass substrate, followed by sputter deposition of Fe (ca. 300 nm) and electron beam evaporation of MgO (ca. 80 nm) through fine-line stencil masks (polyimide (PI), 12.5 µm thick, Kapton, Dupont, USA) defines the electrodes and interconnects, and the gate dielectrics, respectively. Similar procedures yield patterns of sputtered Mg alloy (ca. 100 nm thick, AZ31B) at strategic locations. The different dissolution rates of Fe and Mg alloy lead to a timed sequence of functional transformations initiated by immersion in water. Figure 1b shows images of the system during this transformation. Here, the Mg alloy rapidly dissolves, thereby transforming the function from that of CMOS logic gates (left) to CMOS inverters (right). Magnified views appear in Figure 1c, before (top left, NOR; bottom left, NAND) and after (top/bottom right, CMOS inverters) transformation. Figure 1d presents the electrical characteristics of representative CMOS logic gates (left, NOR; right, NAND) in their initial state; V_A and V_B indicate input voltages; V_{DD} is the supply voltage (10 V). The properties of the CMOS inverters that result from transformation by transience appear in Figure 1e; the gain and threshold voltage (V_{th}) are ca. 50 and 0 V, respectively. The high thresholds of the inverters arise from the high negative threshold voltages (ca. –5 V) of the p-channel MOSFETs. State-of-the-art CMOS device designs can be implemented to reduce the operating voltages. (See additional electrical characteristics of Fe and Mg alloys in Figure S1 in the Supporting Information.)

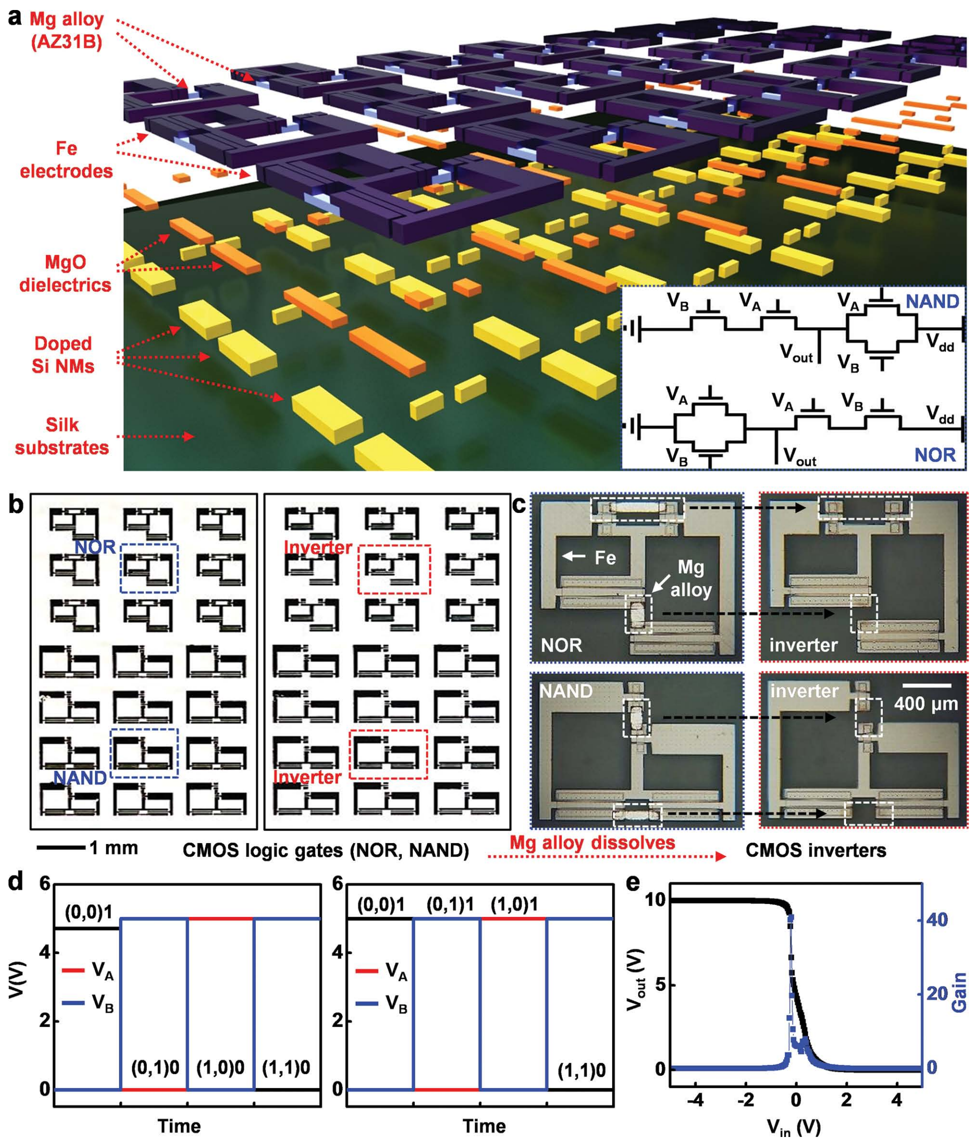

Figure 1. Controlled transformation of function in transient complementary metal-oxide-semiconductor (CMOS) logic gates. a) Schematic exploded view illustration of biodegradable CMOS based logic gates (NAND, NOR), with circuit diagrams in the inset. b) Images of the system before (left, NAND and NOR gates) and after (right, inverters) transformation. c) Magnified images showing functional transformation from logic gates to inverters through dissolution of Mg alloy segments of the interconnect structure. NOR (top left) and NAND (bottom left) gates before transformation, and inverters (top and bottom right) after transformation. d) Output voltage responses of CMOS logic gates. V_A, V_B are the input voltages, and V_{DD} is the supply voltage (10 V). e) Voltage transfer characteristics (VTC) of a representative CMOS inverter after transformation.

Figure 2 shows other examples, in which a patterned encapsulation layer of MgO defines the time sequence of dissolution. Figure 2a–d provides images and electrical properties of CMOS NAND gates, inverters and n-type MOSFETs before and after transformation. In all cases, dissolution of Mg occurs rapidly in regions that do not include the MgO (blue dotted lines). This process changes the NAND gates into inverters and/or into isolated MOSFETs. The system in Figure 2a involves transformation of NAND gates (Figure 2b, left) into inverters (Figure 2b, right). NAND gates (Figure 2c, left) can also be transformed into individual n-channel MOSFETs (Figure 2c, right). Electrical characteristics of the MOSFETs appear in Figure 2d. Transformation of NOR gates (Figure 2e, left) into n-channel MOSFETs (Figure 2e, right) is also possible; Figure 2f shows the properties before and after.

Transient circuits can be functionally transformed not only by separation into individual constituent components, but also by conversion into equivalent systems but with different operation. **Figure 3**a,b shows images and electrical properties of a simple example that combines a serpentine Mg resistor with a Si NM p-n diode, the latter of which is encapsulated with a layer of MgO, before (Figure 3a, left) and after (Figure 3a, right) transformation. In the initial state, most current flows through the resistor because its resistance is much lower than that of the diode at low electrical biases. Dissolution transforms the electrical response from that of a resistor (Figure 3b, left) to a

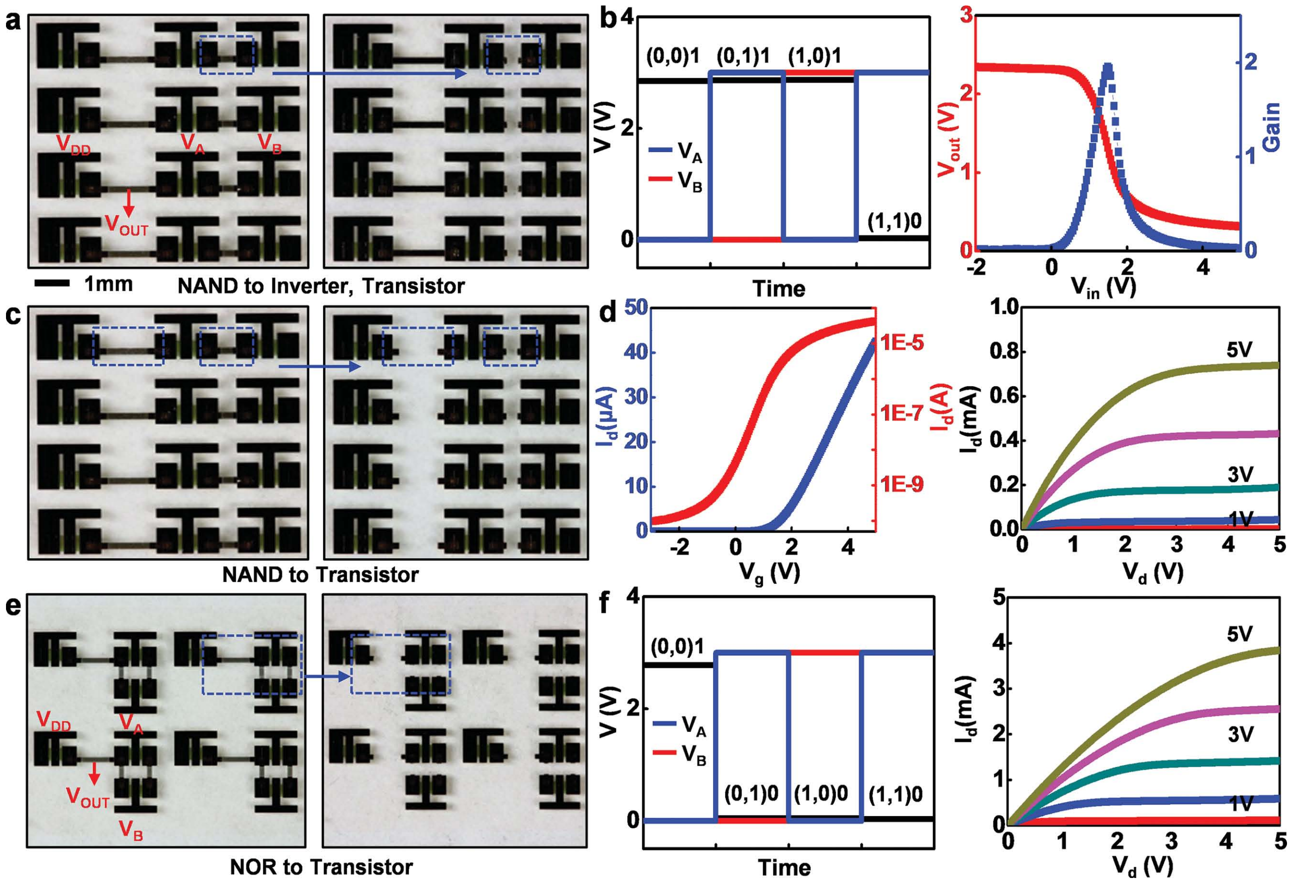

Figure 2. Images and electrical characterization of transient electronic circuits before and after controlled transformation in function. a) Images of transformation from a NAND gate (left) to an inverter and transistor (right) by dissolution of selected parts of the Mg interconnect structure. b) Output voltage responses of a NAND gate (left; V_A and V_B are the input voltages) and voltage transfer characteristics of an inverter after transformation (right). c) Images of transformation from a NAND gate (left) to individual transistors (right) by controlled dissolution of selected parts of the Mg interconnect structure. d) Linear and log scale plots of the transfer curves (left) and current–voltage characteristics (right) of a transistor that results from transformation. e) Images of transformation of a NOR gate (left) into individual transistors (right) by dissolution of selected parts of the Mg interconnect structure. f) Output voltage response of a NOR gate (left) and current–voltage characteristics of a transistor formed by transformation.

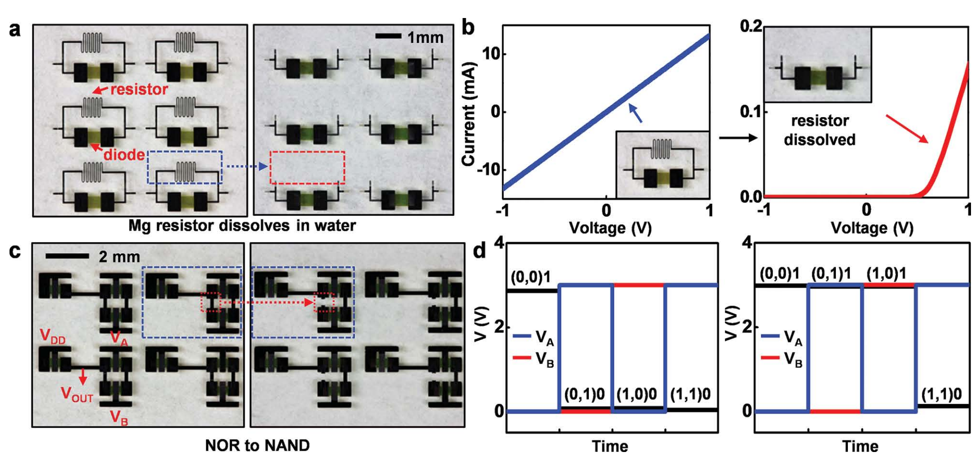

Figure 3. Functional transformation of integrated systems into differentiated sub-systems. a) Images of functional transformation from a resistor (left) to a diode (right) by dissolution of the Mg resistor. b) Current–voltage characteristics of a Mg resistor (left) and a Si NM diode (right). c) Images showing transformation of NOR gates (left) to NAND gates (right) by dissolution of selected parts of the Mg interconnect structure. d) Output voltage responses of the NOR gates (left) and NAND gates (right) shown in (c), with input voltages of V_A and V_B, and a supply voltage of V_{DD} (10 V).

diode (Figure 3b, right). Similar strategies can be used in logic gates. For the case of the device in Figure 3c, the NOR gates (Figure 3c, left) change into NAND gates (Figure 3c, right) through dissolution of certain regions of the interconnects. Figure 3d illustrates corresponding changes in the electrical characteristics, from NOR (left) to NAND (right).

Transformation approaches can also be applied to purely passive components such as radio frequency (RF) antennas and inductive coils for wireless power and communication systems. Here, changes in geometry and/or direction of current flow lead to shifts in the resonance frequencies, directionality patterns and other characteristics. **Figure 4**a summarizes a system that includes a transient Mg antenna connected to a Mg resistor. Certain regions of the antenna, indicated as 'stage 1' (red) and 'stage 2' (blue), are encapsulated with 400-nm and 800-nm-thick layers of MgO, respectively. The other regions are encapsulated with bilayers of MgO (ca. 800 nm) and SiO_2 (ca. 2 µm). The combined use of different materials (e.g., the rate of dissolution of MgO greatly exceeds that of SiO_2,[19] as in Figure S2 in the Supporting Information) and different thicknesses leads to a time sequence of transformation by transience that begins with Mg traces encapsulated by thin MgO. Since the time frame for transformation mainly depends on the dissolution rates of the electrodes, interconnects and/or encapsulation layers, the kinetics can be estimated from separately measured rate of each material.[6,18] Figure 4b shows the maximum temperatures observed during operation of a Mg heater at various stages during its transformation. The frequencies that generate the maximum temperatures correspond to those that lead to the highest energy-conversion

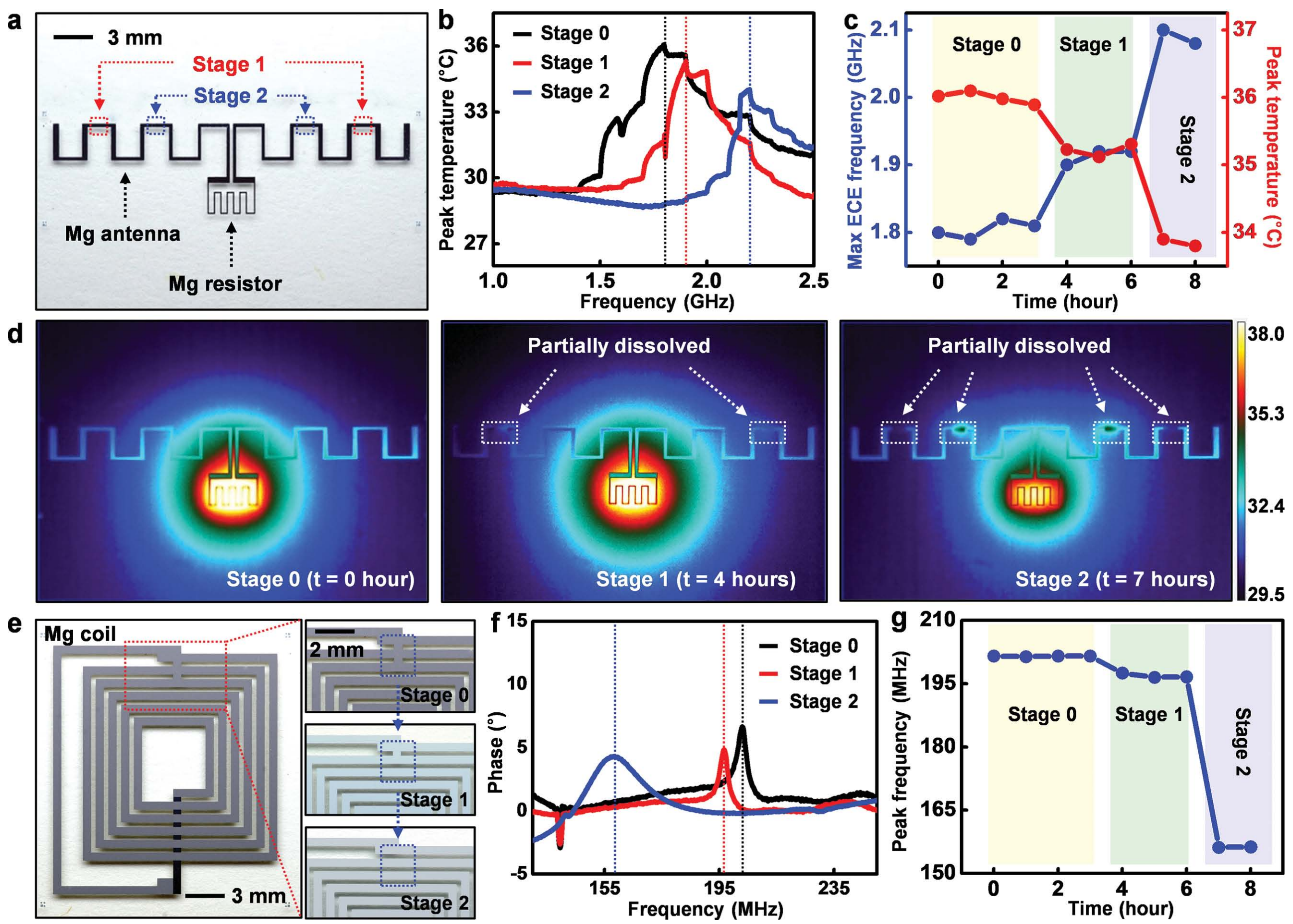

Figure 4. Functional transformation in transient radio frequency (RF) devices. a, Image of a Mg antenna (thickness ca. 2.5 µm) with a Mg serpentine resistor (thickness ca. 2.5 µm). Layers of SiO_2 (ca. 2 µm) and MgO (ca. 800 nm) serve as encapsulation, except in certain regions indicated by the red (stage 1) and blue (stage 2) boxes. b) Variations of the maximum temperature of the resistive heater, evaluated with an IR camera during exposure to RF at different frequencies, for different stages of functional transformation by dissolution in water (black: stage 0, red: stage 1, blue: stage 2). The frequency of maximum energy-conversion efficiency (ECE) (stage 0, 1.8 GHz; stage 1, 1.9 GHz, stage 2, 2.2 GHz) shifts toward higher values as the transformation proceeds from one stage to the next. c) Changes in the frequency for maximum ECE and the peak temperature, evaluated at 1.8 GHz. The results show three separate stages of operation, with time-invariant behaviors for several hours during the first two stages, terminating with rapid degradation. The thicknesses and materials for the encapsulation layers, along with the thickness of the Mg define the timescales at each step. d) Series of IR images of the system at different stages of transformation, captured during exposure to RF at a fixed frequency of 1.8 GHz (the frequency of maximum ECE at stage 0). e) Image of a transient Mg inductor (left) designed to transform in function via dissolution of Mg traces as electrical shorts in the planar spiral coil structure. Magnified views of the device at several stages during transformation (top, stage 0; middle, stage 1; bottom, stage 2). f) Measured changes in the phase response at these different stages (black, stage 0; red, stage 1; blue, stage 2) g, Changes in resonance frequency as a function of time during transformation.

efficiency (ECE) defined by impedance matching. For the case shown here, these frequencies shift from 1.8 GHz (stage 0, black) to 1.9 GHz (stage 1, red) after the outer-most areas (red dotted lines in Figure 4a) dissolve, and to 2.2 GHz (stage 2, blue) by subsequent dissolution of the next outer regions (blue dotted lines in Figure 4a). The shifts in the ECE of the antenna structure compare well to expectation based on simulated results (HFSS, Ansys, USA) in Figure S3a in the Supporting Information (peak shift from 1.82 GHz (stage 0, black) to 1.98 GHz (stage 1, red), to 2.29 GHz (stage 2, blue)). Figure 4c presents changes in the maximum ECE (blue) and the peak temperature (red) as transformations occur via dissolution in deionized (DI) water at 37 °C. The series of infrared (IR) images in Figure 4d indicates a decrease in temperature at the heater for a fixed transmitting frequency (1.8 GHz, optimum value for stage 0), due to reduced ECE (left, stage 0; middle, stage 1; right, stage 2). Since DI water does not include components such as protein, glucose, etc., which exist in human body, the rates of dissolution in a biofluid like human blood are expected to be different. Similar dissolution tests in various solutions, including blood serum, appear in previous reports.[15,16] Figure 4e illustrates a design for a Mg inductor whose resonance frequency transforms via dissolution of local interconnects. Eliminating the crossing lines leads to altered paths for flow of current generated by inductive coupling to a separate primary coil. The resulting changes in turns and geometry of the inductor contribute to a decrease in its resonance frequency. Corresponding electrical properties appear in Figure 4f (black, stage 0, 203 MHz; red, stage 1, 197 MHz; blue, stage 2, 158 MHz). The results agree with simulated values in Figure S3b in the Supporting Information (black, stage 0, 206 MHz; red, stage 1, 196 MHz; blue, stage 2, 159 MHz). Figure 4g presents transformation in the resonance frequency induced by dissolution.

To summarize, the concepts reported here allow well-defined, functional transformation of electronic systems by staged processes in physical transience, as illustrated through water dissolution. Spatially patterned thicknesses and types of encapsulating and/or functional materials provide great versatility in design. The examples show various electrical measurements of high-performance operation, with staged transformation and behaviors that are quantitatively consistent with expectation based on design targets. Such capabilities create unusual opportunities in electronics engineering, where physical changes in the systems induce desired changes in operation, in a way that can complement those of field programmable gate arrays and other established technologies.

Experimental Section

Fabrication Procedures for Si NM-Based CMOS Logic Gates: Doped monocrystalline silicon nanomembranes (Si NMs) (thickness ca. 260 nm, n-type) derived from silicon-on-insulator (SOI) (SOITEC, France) wafers formed the active areas of the semiconductor devices. Spin-on dopants (SODs) (Filmtronics, USA) applied with different annealing temperatures yielded the respective p^-, n^+ and p^+ doped regions for the p wells, and for the source and drain electrodes of the p- and n-channel metal-oxide-semiconductor field-effect transistors (MOSFETs). The lateral dimensions of the active device regions of the Si NMs were defined by reactive ion etching (RIE) with sulfur hexafluoride (SF_6) gas. To release Si NMs from the SOI, the buried oxide was partially removed underneath the patterned Si, and completely eliminated in the other areas by etching with hydrofluoric acid (HF) (ScienceLab, USA). A thin, patterned layer of photoresist (AZ 5214) formed anchor bars to tether the Si NMs to the wafer during removal of the remaining buried oxide with an additional etching step. The patterned Si NMs were then transfer printed onto a glass substrate coated with a thin layer of silk. Evaporation of MgO (ca. 80 nm) through a polyimide shadow mask formed layers that served as gate dielectrics. Source, drain, and gate electrodes, as well as interconnects (Fe, ca. 300 nm) were defined by a similar process, followed by deposition of Mg alloy (AZ31B, ca. 100 nm) into selected areas to complete the system.

Preparation of Crystallized Silk Films: Aqueous silk solution was prepared by boiling the cocoons of *Bombyx mori* in 0.02 M sodium carbonate for 30 min to remove the sericin. The remaining fibroin was rinsed in DI water and allowed to dry overnight, before dissolution in 9 M lithium bromide (LiBr) for 4 h at 60 °C. The resulting solution was dialyzed for 36 h against DI to remove the salt, yielding a 7% aqueous solution of silk fibroin.[20] Glass slides that had been exposed briefly to an oxygen plasma (50 W, 30 s, 100 sccm O_2) served as substrates for casting 0.25 mL/in^2 of solution. The films were allowed to dry at ambient conditions before crystallization by water-vapor annealing for 24 h at room temperature.[21–23] The resulting films were served as substrates in subsequent fabrication steps.

Fabrication of Mg Antennas and Inductors: Traces of Mg deposited by electron-beam evaporation (ca. 2.5 µm) formed antennas and serpentine resistive heaters connected to antennas. The crossovers and spiral coils for the inductors were defined by electron-beam evaporation of Mg (ca. 2.5 µm), and plasma-enhanced chemical vapor deposition (PECVD) of SiO_2 (ca. 900 nm). Both devices (i.e., antennas and inductors) were encapsulated with a thick layer of PECVD SiO_2 (ca. 2 µm), followed by the removal of certain patterned regions of this oxide. Different thicknesses of MgO (ca. 400 nm and ca. 800 nm) were deposited at these locations.

Electrical Characterization of Functional Transformation by Controlled Transience in Antennas and Inductors: The radio frequency (RF) characteristics of the Mg antennas and inductors were measured every hour after immersion in DI water at 37 °C. Samples were removed from the solutions, dried, and measured at each stage for the purpose of electrical characterization. Absorption of RF was inferred from temperatures evaluated using an infrared (IR) camera. The power and distance were fixed at 30 W and 5 cm, respectively; the frequency was varied between 1 GHz to 2.5 GHz. The energy-conversion efficiency (ECE) at each distinct stage of transformation was defined at the frequency that yielded the maximum temperature (1.8 GHz) in the initial configuration. The shifts in resonance frequency of the antennas, caused by dissolution of Mg, led to a decrease in temperature. The resonance frequency of the transient inductor was evaluated by near-field coupling to a circular primary coil (diameter ca. 2 cm) connected to an impedance analyzer.[24] The phase shift was determined by sweeping the frequency of the primary coil from 120 to 250 MHz. The peak position defined the resonance frequency.

Supporting Information

Supporting Information is available from the Wiley Online Library or from the author.

Acknowledgements

S.-W.H., S.-K.K. and X.H. contributed equally to this work. M.A.B would like to thank the American Society for Engineering Education and the office of Naval Research for their support through the NDSEG fellowship. This material is based upon work supported by the Defense Advanced Research Projects Agency.

Received: July 8, 2014
Revised: September 11, 2014
Published online: October 30, 2014

[1] D.-H. Kim, Y.-S. Kim, J. Amsden, B. Panilaitis, D. L. Kaplan, F. G. Omenetto, M. R. Zakin, J. A. Rogers, *Appl. Phys. Lett.* **2009**, *95*, 133701.
[2] D.-H. Kim, J. Viventi, J. Amsden, J. Xiao, L. Vigeland, Y.-S. Kim, J. A. Blanco, B. Panilaitis, E. S. Frechette, D. Contreras, D. L. Kaplan, F. G. Omenetto, Y. Huang, K.-C. Hwang, M. R. Zakin, B. Litt, J. A. Rogers, *Nat. Mater.* **2010**, *9*, 511.
[3] C. J. Bettinger, Z. Bao, *Adv. Mater.* **2010**, *22*, 651.
[4] M. Irimia-Vladu, P. A. Troshin, M. Reisinger, L. Shmygleva, Y. Kanbur, G. Schwabegger, M. Bodea, R. Schwödiauer, A. Mumyatov, J. W. Fergus, V. F. Razumov, H. Sitter, N. S. Sariciftci, S. Bauer, *Adv. Funct. Mater.* **2010**, *20*, 4069.
[5] M. Irimia-Vladu, P. A. Troshin, M. Reisinger, G. Schwabegger, M. Ullah, R. Schwoediauer, A. Mumyatov, M. Bodea, J. W. Fergus, V. F. Razumov, H. Sitter, S. Bauer, N. S. Sariciftci, *Org. Electron.* **2010**, *11*, 1974.
[6] S.-W. Hwang, H. Tao, D.-H. Kim, H. Cheng, J.-K. Song, E. Rill, M. A. Brenckle, B. Panilaitis, S. M. Won, Y. S. -Kim, Y. M. Song, K. J. Yu, A. Ameen, R. Li, Y. Su, M. Yang, D. L. Kaplan, M. R. Zakin, M. J. Slepian, Y. Huang, F. G. Omenetto, J. A. Rogers, *Science* **2012**, *337*, 1640.
[7] M. Irimia-Vladu, E. D. Glowacki, P. A. Troshin, G. Schwabegger, L. Leonat, D. K. Susarova, O. Krystal, M. Ullah, Y. Kanbur, M. A. Bodea, V. F. Razumov, H. Sitter, S. Bauer, N. S. Sariciftci, *Adv. Mater.* **2012**, *24*, 375.
[8] Y. J. Kim, S.-E. Chun, J. Whitacre, C. J. Bettinger, *J. Mater. Chem. B* **2013**, *1*, 3781.
[9] Y. J. Kim, W. Wu, S.-E. Chun, J. F. Whitacre, C. J. Bettinger, *Proc. Natl. Acad. Sci. USA* **2013**, *110*, 20912.
[10] M. Irimia-Vladu, *Chem. Soc. Rev.* **2014**, *43*, 588.
[11] S.-W. Hwang, J.-K. Song, X. Huang, H. Cheng, S.-K. Kang, B. H. Kim, J.-H. Kim, S. Yu, Y. Huang, J. A. Rogers, *Adv. Mater.* **2014**, *26*, 3905.
[12] L. Yin, X. Huang, H. Xu, Y. Zhang, J. Lam, J. Cheng, J. A. rogers, *Adv. Mater.* **2014**, *26*, 3879.
[13] S.-W. Hwang, X. Huang, J.-H. Seo, J.-K. Song, S. Kim, S. Hage-Ali, H.-J. Chung, H. Tao, F. G. Omenetto, Z. Ma, J. A. Rogers, *Adv. Mater.* **2013**, *25*, 3526.
[14] S.-W. Hwang, D.-H. Kim, H. Tao, T.-I. Kim, S. Kim, K. J. Yu, B. Panilaitis, J.-W. Jeong, J.-K. Song, F. G. Omenetto, J. A. Rogers, *Adv. Funct. Mater.* **2013**, *23*, 4087.
[15] S.-W. Hwang, G. Park, C. Edwards, E. A. Corbin, S.-K. Kang, H. Cheng, J.-K. Song, J.-H. Kim, S. Yu, J. Ng, J. E. Lee, J. Kim, C. Yee, B. Bhaduri, Y. Su, F. G. Omennetto, Y. Huang, R. Bashir, L. Goddard, G. Popescu, K.-M. Lee, J. A. Rogers, *ACS Nano* **2014**, *8*, 5843.
[16] S.-W. Hwang, G. Park, H. Cheng, J.-K. Song, S.-K. Kang, L. Yin, J.-H. Kim, F. G. Omenetto, Y. Huang, K.-M. Lee, J. A. Roger, *Adv. Mater.* **2014**, *26*, 1992.
[17] C. Dagdeviren, S.-W. Hwang, Y. Su, S. Kim, H. Cheng, O. Gur, R. Haney, F. G. Omenetto, Y. Huang, J. A. Rogers, *Small* **2013**, *9*, 3398.
[18] L. Yin, H. Cheng, S. Mao, R. Haasch, Y. Liu, X. Xie, S.-W. Hwang, H. Jain, S.-K. Kang, Y. Su, R. Li, Y. Huang, J. A. Rogers, *Adv. Funct. Mater.* **2014**, *24*, 645.
[19] S.-K. Kang, S.-W. Hwang, H. Cheng, S. Yu, B. H. Kim, J.-H. Kim, Y. Huang, J. A. Rogers, *Adv. Funct. Mater.* **2014**, *24*, 4427.
[20] D. N. Rockwood, R. C. Preda, T. Yücel, X. Wang, M. L. Lovett, D. L. Kaplan, *Nat. Protoc.* **2011**, *6*, 1612.
[21] X. Hu, K. Shmelev, L. Sun, E. S. Gil, S. H. Park, P. Cebe, D. L. Kaplan, *Biomacromolecules* **2011**, *12*, 1686.
[22] X. Hu, D. L. Kaplan, P. Cebe, *Macromolecules* **2008**, *41*, 3939.
[23] X. Hu, D. L. Kaplan, P. Cebe, *Thermochim. Acta* **2007**, *461*, 137.
[24] X. Huang, Y. Liu, H. Cheng, W.-J. Shin, J. A. Fan, Z. Liu, C.-J. Lu, G.-W. Kong, K. Chen, D. Patnaik, S.-H. Lee, S. Hage-Ali, Y. Huang, J. A. Rogers, *Adv. Funct. Mater.* **2014**, *24*, 3846.

